DNA-based nanocarriers to sequester altered microRNAs in cardiac dysfunction

Alejandro Postigo[1‡], Natalia Hernández-Bellido[2,3‡], Marcos Sánchez-Barat[2,3], Laura García-Mendívil[2,3], Esther Pueyo[2,3,4], Jesús del Barrio[1], Silvia Hernández-Ainsa[1,5]*, Laura Ordovás[2,3,5, 6]*

‡ These authors contributed equally

1. Instituto de Nanociencia y Materiales de Aragón (INMA), CSIC-Universidad de Zaragoza, 50009, Spain

2. Instituto de Investigación en Ingeniería de Aragón (I3A), Universidad de Zaragoza, Zaragoza, 50018, Spain

3. Instituto de Investigación Sanitaria (IIS) Aragón, Zaragoza, 50009, Spain

4. Centro de Investigación Biomédica en Red de Bioingeniería, Biomateriales y Nanomedicina (CIBER-BBN)

5. Fundación ARAID, Gobierno de Aragón, Zaragoza, 50018, Spain

6. Biomedical Research Networking Center in Bioengineering, Biomaterials and Nanomedicine (CIBER-BBN), Zaragoza, 50018, Spain

KEYWORDS

22 **ABSTRACT**

23 MicroRNAs (miRs) play a critical role in modulating gene expression across biological processes,

24 including cardiac aging and disease. As such, miRs have demonstrated therapeutic potential in

25 several cardiac conditions. Efficient delivery of miR therapies to cardiac tissue is crucial for

26 effective gene therapy and DNA-based nanocarriers (DNCs), based on Watson-Crick-Franklin

27 highly specific base-pair recognition, have emerged as a promising, biocompatible alternative to

28 viral-based methods.

29 Here, we present DNCs designed to modulate miR levels as a potential treatment for cardiac

30 dysfunction. Specifically, our DNCs target miR-24-2, which inhibits SERCA2 gene. In humans,

31 the reduction of SERCA2 activity is a hallmark of heart failure and is altered in cardiac aging. We

32 show how DNCs bearing anti-miR-24-2-5p sequences effectively restore intracellular levels of

33 SERCA2 in a HEK293 cell model. Here, the DNCs proper assembly is thoroughly verified, while

34 their stability and miR-capture ability are demonstrated in vitro. Our anti-miR-24-2-5p DNCs

35 exhibit successful internalization into HEK293 and modest uptake into human cardiomyocytes.

36 SERCA2 restoration by DNCs is significantly influenced by the miR-capture sequence layout,

37 underscoring the importance of precise design for optimal biological outcomes. This study

38 highlights the potential of DNCs in cardiac therapies, a previously unexplored avenue for

39 addressing cardiac dysfunction.

INTRODUCTION

Cardiovascular disease (CVD) currently stands as the foremost cause of global mortality and morbidity, accounting for approximately 17.9 million deaths per year and constituting 32% of all-cause mortality.[1] Age is an independent risk factor for CVD, which is intricately linked to other pathological processes.[2] Therefore, the aging of the population, coupled with the prevalence of comorbidities, is expected to further consolidate and potentially exacerbate this epidemiological burden.[2,3] Moreover, the development of novel therapeutic approaches for the treatment of CVD is lagging behind, hampered by a lack of an in-depth understanding of the molecular pathways governing cardiac dysfunction.

miRs play a crucial role in regulating gene expression in many biological processes, including CVD and cardiac aging.[4–6] Due to their small size and pleiotropic effects, miRs are emerging as promising therapeutics. Consequently, the modulation of cardiac miRs has demonstrated reparative and regenerative potential in the heart. For example, improved cardiac function in animal models of heart failure (HF) or myocardial infarction (MI)[7,8] has been reported and even a first-in-human trial in HF shows safety and cardiac functional improvements.[9]

miR-24-2 is upregulated in HF patients[10] and in aged human left ventricle (LV).[6] In addition, it is also implicated in the regulation of post-MI cardiac fibrosis.[11,12] miR-24-2-5p interacts with *SERCA2*,[6] a fundamental pump located in the sarcoplasmic reticulum of cardiomyocytes and whose activity is critical for controlling cardiac contractility and relaxation. Opposite to miR-24-2, *SERCA2* levels decrease with age and in HF.[6,13] Restoring SERCA2 levels currently represents a key pathway in gene therapy to address failing hearts[13] with several completed or ongoing *SERCA2* supplementation gene therapy trials (i.e. CUPID, MUSIC-HFrEF or MUSIC-HFpEF). All of these trials are based on *SERCA2* delivery with Adeno-Associated Virus serotype 1 (AAV1),

63   however, the existence of AAV1 neutralizing antibodies in humans[14] could compromise their

64   success. Therefore, using non-viral methods to restore SERCA2 activity by inhibiting miR-24 in

65   the cardiac tissue is a promising strategy for the treatment of cardiac dysfunction.

66   The direct administration of miR-regulatory therapies has exhibited only limited efficacy in human

67   clinical trials for HF.[9] Likely limitations related to their nuclease sensitivity or rapid clearance

68   limit effective dosing in the cardiac tissue. Additionally, systemic distribution of such approaches

69   have been associated with adverse side effects in other pathologies.[15] In light of these limitations,

70   nanocarriers are being avidly used to enhance the intracellular delivery of therapeutic nucleic

71   acids, with the aim of improving the *in vivo* efficacy and safety of miR therapies.[16]

72   DNA-based nanocarriers (DNCs) have emerged as promising candidates for efficient delivery of

73   miRs *in vivo*. Constructed using a bottom-up approach that relies on highly specific and

74   programmable self-assembly of individual DNA oligonucleotides, DNCs have exhibited

75   biocompatibility at the cellular level as well as in animal models,[14] with no systemic toxicity and

76   low immunogenic response[17]. These favorable properties, combined with their straightforward

77   and reproducible preparation, versatile design, functionality and facile adaptability for targeted

78   delivery, make DNCs suitable vehicles for therapeutic delivery in various applications, including

79   chemotherapy,[18] gene therapy[19,20] or immunotherapy[21] among others. The chemical backbone

80   of DNCs makes them particularly suited for gene delivery, as it can be tailored to harbor

81   therapeutic sequences, such as antisense oligonucleotides (ASOs), messenger RNAs, miR mimics,

82   anti-miRs and small interfering RNAs (siRNAs).[19]

83   In the context of miR-related therapy, DNA nanocages with truncated octahedral shapes,[22] RCA-

84   based DNA nanosponges,[23] branched DNA nanostructures[24–26] and a DNA tetrahedron[27] have

85   successfully inhibited oncogenic miRs within cells. *In vivo* efficacy has been also provided by 3-

86 way junction RNA nanoparticles that efficiently reduce the activity of oncogenic miR-21 and miR-

87 17 in mice,[28,29] by DNA tetrahedron loaded with miR inhibitors for skin anti-aging properties[30]

88 and for miR-22-3p carriers to address a depressive disorder.[31] Additionally, hybrid miR-

89 containing DNA tetrahedron and hydrogel systems have shown *in vivo* effect in tackling

90 osteonecrosis through combined therapy.[32] While these examples highlight the potential of DNCs

91 for miR-based therapies in cancer, it is noteworthy that their use in treating cardiac diseases

92 remains unexplored.

93 Here, we present DNCs tailored to address cardiac dysfunction with miR therapies, in particular

94 with application in HF or to mitigate the deleterious effects of cardiac aging. Specifically, our

95 DNCs are designed to modulate the intracellular levels of miR-24-2-5p using an anti-miR approach

96 and consequently, the levels of SERCA2. We have designed and fully characterized two different

97 DNC configurations differing in the position of the miR bait, and thus in the miR capture strategy.

98 Our data demonstrate the proper assembly of both DNC configurations, the specific capture of the

99 target miR and subsequent DNCs disassembly, and their proper stability in biological conditions

100 *in vitro*, among other features. Interestingly, only one configuration is able to rescue the

101 intracellular levels of SERCA2 in a model cell system. Our anti-miR-24-2-5p DNCs are able to

102 internalize at low levels in human induced pluripotent stem cell-derived cardiomyocytes (iCMs)

103 *in vitro*, underscoring the opportunity to develop methods to enhance their cell-specific uptake *in*

104 *vivo*.

RESULTS AND DISCUSSION

Design, assembly, structural characterization and nuclease-mediated degradation of anti-miR-containing DNCs

DNCs were prepared through complementary hybridization of smaller building block units (Figure 1) to render nanohydrogel-type nanostructures by adapting previous methods.[33]
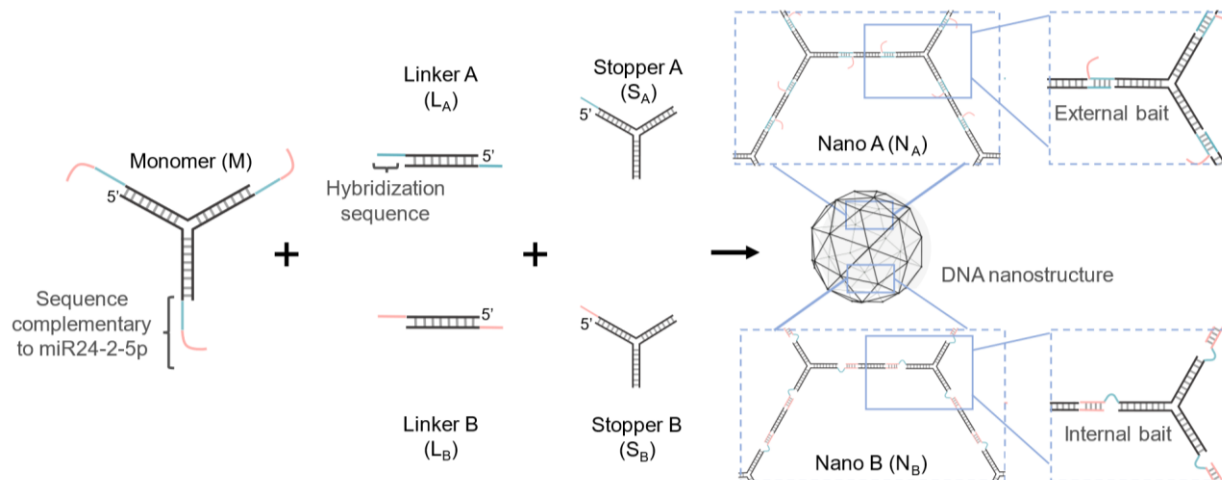
Figure 1. DNCs assembly in their two configurations (N_A and N_B). Complementary sequences between monomer, linker and stopper overhangs are shown in either blue (N_A) or red (N_B). DNCs were assembled by mixing M, S and L following the ratio 64:1 (M:S), 1:1.5 (M:L) and 2:1 (S:L).

Initially, two Y-shaped DNA constructs, Monomer (M) and Stopper (S), each composed by three complementary strands, and one double-stranded DNA serving as linker (L), were assembled in a phosphate saline buffer (PBS) using a thermal gradient. M comprises three dsDNA arms ending in 22-nucleotides (nts) long overhangs fully complementary to the target miR-24-2-5p, thereby acting as anti-miR-24-2-5p. L hybridizes with 12-nts of these overhangs to drive the assembly of the entire DNC. The non-hybridized 10 nts of M act as bait for miR capture. S contains a 12 nts-long overhang in just one arm to block DNC growth. Two types of DNCs were prepared by

122 modifying the position at which L bridges the monomers. Namely, the DNC_A (N_A) was assembled

123 with L hybridizing with the internal part of the M overhang, leaving a 10 nts long external bait.

124 Conversely, DNC_B (N_B) was assembled with L hybridizing with the external part of the M

125 overhang, leaving a 10 nts long internal bait (Figure 1, Table S1).

126 Polyacrylamide gel electrophoresis (PAGE), Dynamic Light Scattering (DLS) and Atomic Force

127 Microscopy (AFM) were employed to assess the proper formation of DNCs. In PAGE (Figure 2a),

128 distinct bands for M, S and L were observed and their mobility, following the order L>S>M,

129 correlated with their respective structural sizes. For N_A and N_B lanes, DNA signals were visibly

130 retained in the wells, smearing toward faster mobility species, indicating correct assembly of small

131 components into larger structures. Agarose gel electrophoresis (AGE) further confirmed correct

132 assembly (Figure S1), as evidenced by the retarded mobility of DNCs compared to the smaller

133 DNA constructs. DLS data (Figure 2b) and AFM images (Figure 2c) showed increased sizes for

134 the DNCs compared to M. Specifically, average hydrodynamic diameters (Dh) of 81 ± 26 nm, 67

135 ± 15 nm and 12 ± 2 nm were obtained by DLS for N_A, N_B and M, respectively, with larger standard

136 deviation observed for N_A (Figure 2b, S2a). The 10 nts long internal bait present in N_B introduces

137 larger flexibility and hence may facilitate the hybridisation of the linker leading to a narrower size

138 distribution. AFM images taken in dry samples revealed larger averaged sizes for N_A (34 ± 12 nm)

139 and N_B (28 ± 9 nm) compared to M (10 ± 2 nm) (Figure S2b). The smaller values obtained by

140 AFM compared by DLS may arise from tip compression of the nanostructures, as well as potential

141 compaction of the nanohydrogel-type DNCs in the absence of water.[34–37] DNCs displayed a

142 globular-like morphology in AFM images, which is consistent with the expected structural design

143 for these nanostructures.[33,38,39]

DNCs' biodegradability was studied by evaluating their susceptibility to nuclease-mediated degradation by DNAse I, a major nuclease present in serum.[40] PAGE analysis showed that N_A, N_B and M are all degraded by DNAse I (Figure S3), confirming their optimal degradation in biological conditions and supporting their potential as safe, biodegradable nanocarriers.
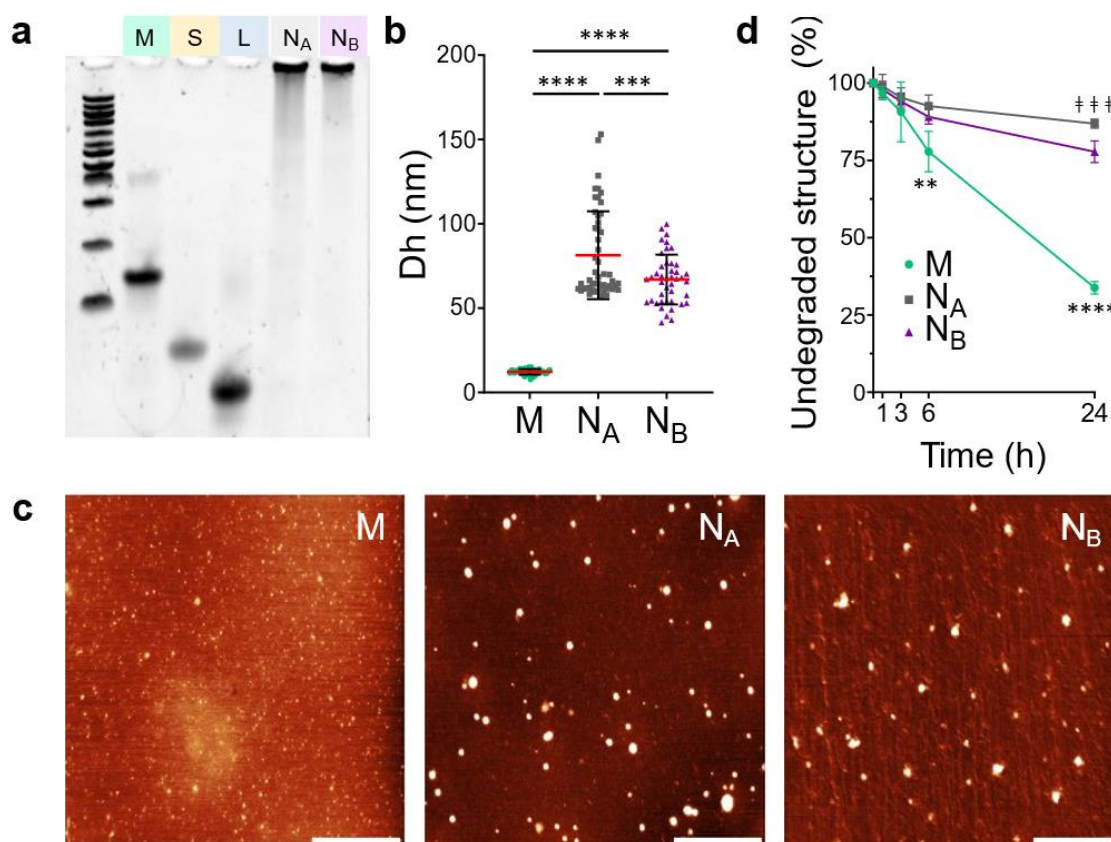
Figure 2. Characterization of the DNCs. a) PAGE showing retarded mobility of the assembled N_A and N_B compared to M, S and L. 100 bp DNA ladder is included at the most left lane. b) Distribution of the hydrodynamic diameter (Dh) values (in intensity) obtained by DLS of M, N_A and N_B (individual values and mean ± SD; n = 5 independent studies of 10 measurement each). c) AFM images (topography) of M, N_A and N_B. Scale bar is 500 nm; d) Percentage of intact nanostructures incubated in cell culture media with serum over time in hours (h) (mean ± SD; n =

155   3-4; * for comparison of M with both N_A and N_B; ‡ for comparison of N_A with N_B). Significant

156   thresholds were established at: $p \leq 0.05$ (*), $p \leq 0.01$ (**), $p \leq 0.001$ (***) and $p \leq 0.0001$ (****).

157

158   Next, to assess whether the DNCs maintain their structural integrity under the chemical conditions

159   relevant to subsequent investigations with cultured cells, we analysed the stability of the DNCs in

160   cell culture media containing 10% of FBS (DMEMc) for different times up to 24 hours (h) at 37

161   ºC. A notable degradation of M in DMEMc at 24 h (only $34 \pm 2\%$ of intact structure remaining)

162   indicated the vulnerability in serum of the building unit. Instead, N_A and N_B displayed good

163   stability in DMEMc up to 24 h ($87 \pm 2\%$ and $78 \pm 4\%$ of non-degraded structure, respectively),

164   with N_A being significantly more stable than N_B at 24 h (Figure 2d and Figure S4a). Stability

165   controls were performed by incubating the structures in nuclease-free PBS for 24 h at 37 ºC (Figure

166   S4b), and all structures remained stable, confirming their robustness under nuclease-free

167   physiological conditions. The higher stability of N_A and N_B compared to M in DMEMc, highlights

168   the enhanced protection of the anti-miR sequences by the assembled DNCs in biological media.

169   Therefore, the designed building units self-assemble into DNA nanohydrogel-type structures

170   bearing anti-miR-24-2-5p sequences with Dh of around 75 nm. These DNCs are biodegradable

171   but stable in cell culture conditions during 24 h.

172

173   **Specific capture of miR-24-2-5p by DNCs**

174   Prior to the functional assessment in cells, the capability of the assembled DNCs to specifically

175   sequester miR-24-2-5p was evaluated *in vitro* using PAGE and fluorescence spectroscopy.

176   According to the DNCs design (Figure 1), N_A and N_B are assembled through the hybridization of

177   M with L via 12 complementary nts of M extension over a total of 22 nts. Hence, in the presence

178   of miR 24-2-5p, L is expected to be displaced from M by the miR via toehold-mediated strand

179   displacement, which results into DNCs disassembly. This design of miR-triggered disassembling

180   nanostructures provides an intrinsic structural reporter to confirm successful miR capture.

181   Furthermore, upon recognition of the target miR, the unoccupied anti-miR sequences of inner

182   locations within the DNCs improve their exposure, subsequently potentially increasing the

183   accessibility of the miR to the baits. Finally, this system is expected to facilitate RNase H-mediated

184   degradation of the resulting DNA-RNA heteroduplex in the intracellular media. To probe this

185   disassembly, N_A and N_B were incubated for 1 h at 37 ºC in PBS with the miR-24-2-5p target

186   sequence as either single-stranded DNA (ssDNA) or RNA (ssRNA) (Table S1). Incubation of M

187   with each target sequence in a molecular ratio anti-miR bait:target strand 1:2 resulted in gel

188   migration retardation of M, supporting effective capture (Figure 3a). In the case of N_A and N_B, the

189   non-migrating band of the fully assembled DNCs nearly vanished upon incubation with the target

190   strands at this ratio. Instead, a band corresponding to M with the captured ssDNA or ssRNA was

191   observed, with just a few complexes of smaller size than the original fully assembled DNCs

192   present, which supports successful disassembly of both DNCs (Figure 3a).

193   The addition of ssRNA at ratio 1:1 (anti-miR bait:target strand) also led to proper disassembly of

194   DNCs, whereas lower molar ratios resulted in only partial disassembly (Figure S5). The specificity

195   of the interaction was further validated by employing a single-stranded DNA sequence with a

196   random anti-miR sequence with no homology to miR-24-2-5p ($ssDNA_{mock}$) (Table S1). Neither M

197   nor the DNCs exhibited any interaction with $ssDNA_{mock}$, supporting the selectivity of the bait

198   specifically toward miR-24-2-5p (Figure 3a).

199
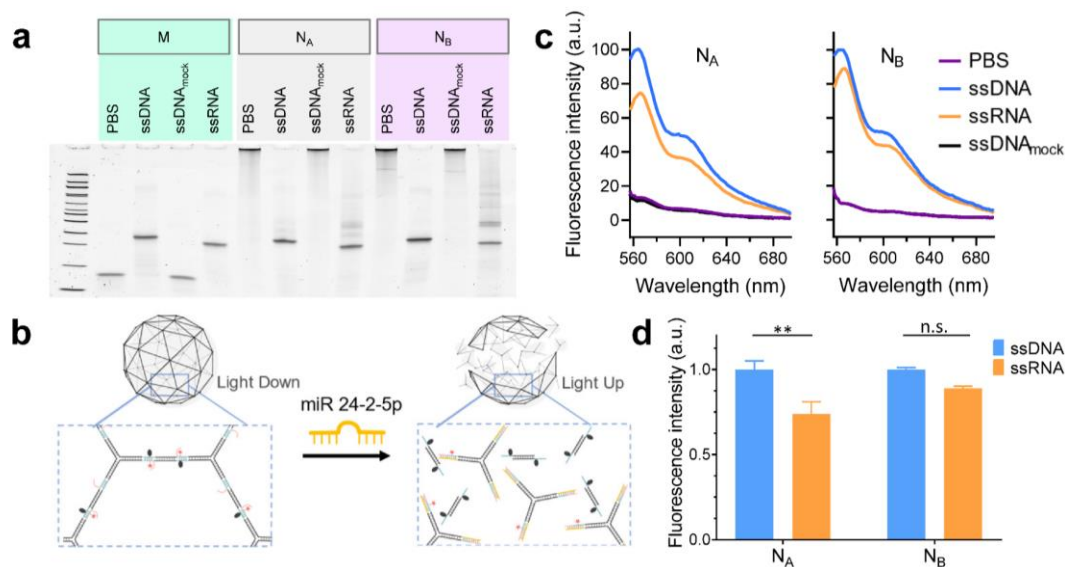
Figure 3. Assessment of capture capacity and specificity of miR-24-2-5p by DNCs. a) PAGE showing interaction of M with the target sequence (as ssDNA, ssRNA) and disassembly of N_A and N_B with the target sequence (as ssDNA and ssRNA) and random sequence (ssDNA$_{mock}$) at ratio 1:2 of anti-miR bait:ssDNA/ssRNA/ssDNA$_{mock}$). 100 bp DNA ladder is included at the most left lane. b) DNCs$_{LU}$ design with fluorescence up detection capacity for disassembly. c) Fluorescence spectra of DNCs$_{LU}$ upon incubation at 37 ºC for 1 h with ssRNA and ssDNA target sequences and ssDNA$_{mock}$ (ratio 1:2 anti-miR bait: target strand). d) Fluorescence fold enhancement of DNCs after incubation with the target ssDNA or ssRNA sequences at a ratio 1:2 anti-miR bait: target strand. Values are normalized by the enhancement observed for ssDNA for each DNC (mean ± SD; n = 3). Significance thresholds were established at: $p \leq 0.05$ (*), $p \leq 0.01$ (**), $p \leq 0.001$ (***) and $p \leq 0.0001$ (****).

211

Fluorescence spectroscopy was also employed to quantitatively assess the degree of target sequence capture and its selectivity under physiological temperature (37 ºC). To this end, DNCs were designed to hold a Cy3 fluorophore and a BMN-Q535 dark quencher (Figure S6). Assembled

11

215 DNCs present quenched Cy3 fluorescence (light down), while disassembly results in unquenching

216 and Cy3 fluorescence emission (light up) (Figure 3b). These fluorescent light down/up DNCs,

217 hereafter referred to as DNC_{LU}, were incubated for 1 h at 37 ºC with the miR-24-2-5p target

218 sequence at 1:2 ratio of anti-miR bait:target strand sequences (Figure 3c-d). Fluorescence intensity

219 was significantly increased for both $DNCs_{LU}$ upon incubation with both ssDNA and ssRNA,

220 whereas no substantial enhancement was observed in the case of the $ssDNA_{mock}$ control (Figure

221 3c). This result confirmed the specific capability of both $DNCs_{LU}$ to capture the miR-24-2-5p target

222 sequence. The increase in fluorescence signal for N_A in presence of ssRNA was significantly lower

223 than for ssDNA, while fluorescence enhancement for N_B was equally substantial for both ssRNA

224 and ssDNA (Figure 3c-d). This data suggests a more efficient ssRNA-mediated disassembly in the

225 case of N_B than N_A, and hence more efficient capture of the specific miR sequence by N_B than by

226 N_A at physiological temperature. Differences in the stability of the newly formed RNA-DNA

227 heteroduplex could explain this observation. Indeed, Tm values from the DNA-DNA duplex

228 fragment between M and L (before displacement) and from DNA-RNA heteroduplex fragment

229 between M and ssRNA (after displacement) are much enhanced in N_B compared to N_A, which may

230 facilitate the disassembly (Figure S7). Also, steric hindrance may account for this difference,[42]

231 with the external bait (in N_A) producing more steric hindrance for the approach of ssRNA than the

232 internal bait (in N_B).

233 Overall, both DNCs demonstrated the capacity to specifically capture the miR target sequence *in*

234 *vitro* at 37 ºC.

235 **Cell viability, intracellularly stability and cell internalization**

236 Next, we investigated the DNCs bioactivity *in vitro*. A routine cell line with no expression of miR-

237 24-2-5p, namely HEK293, was chosen as a model system to demonstrate the functionality of the

238 customized DNCs. Cell proliferation of HEK293 treated with M, N_A and N_B in DMEMc for up to

239 24 h paralleled the one of untreated cells (Figure S8), confirming the lack of cytotoxicity of all the

240 structures.

241 The internalization capacity in HEK293 of our Cy3-labelled DNCs was evaluated by flow

242 cytometry at different time points for up to 48 h in terms of proportion of loaded cells (Figure 4a

243 and Figure S9b) and loading capacity (Figure 4b). Both Cy3-labelled DNCs, N_A and N_B, were

244 avidly internalized after 7 h of incubation, with more than 50% of $Cy3^+$ cells observed (Figure 4a).

245 They displayed though a low DNC load, as indicated by the nearly unnoticed increase in the Cy3

246 mean fluorescence intensity (MFI) (Figure 4b). After 24 h of incubation, 100% of the cells had

247 internalized Cy3-labelled DNCs and showed an average of more than 3-fold increase in the DNC

248 load per cell compared to the initial time point. Beyond 24 h, the uptake persisted reaching more

249 than 10-fold increase in load. Both N_A and N_B showed comparable internalization capabilities in

250 the HEK293 model cell system.
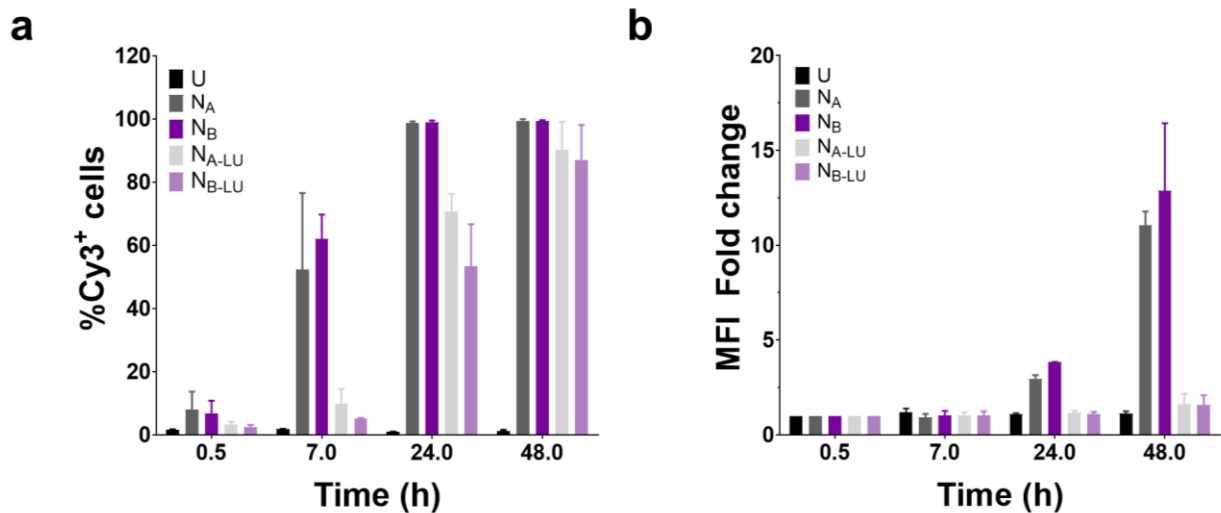
251

252 **Figure 4.** Kinetic of cellular uptake and intracellular stability of anti-miR fragments of DNCs in

253 HEK293 cells. a) Percentage of $Cy3^+$ cells in the presence of Cy3-labelled DNCs or $DNCs_{LU}$

254 compared to untreated (U) cells reporting uptake or anti-miR trap degradation, respectively. b)

255   Levels of average Cy3 fluorescence per cell (Mean fluorescence, MFI) in the presence of Cy3-

256   labelled DNCs or DNCs$_{LU}$ compared to untreated (U) cells reporting uptake or degradation,

257   respectively (mean±SD n = 2 with 3-4 technical replicates each).

258

259   The intracellular stability of DNCs was tracked using the DNCs$_{LU}$ system (used previously to

260   assess the efficiency of miR capture by DNCs in Figure 3c-d and Figure S6) and exploiting the

261   lack of expression of miR-24-2-5p in HEK293 cells, which rules out the DNCs disassembly

262   specifically triggered by the miR. In this system, the increase in fluorescence signal can be related

263   to the intracellular degradation of the functional anti-miR fragments of DNCs$_{LU}$. As such, the

264   proportion of cells with intracellular degradation of both N$_{A-LU}$ and N$_{B-LU}$ gradually rose over time

265   following the uptake trend and reaching almost 100% of cells harboring degraded DNCs at 48 h

266   (Figure 4a). However, the amount of degraded DNCs per cell of both structures (N$_{A-LU}$ and N$_{B-LU}$)

267   remained minimal compared to the initial time point and the total DNC load (Cy3-DNCs) (Figure

268   4b). No significant differences in the intracellular stability were observed between N$_{A-LU}$ and N$_{B-}$

269    $_{LU}$ (Figure S9). Altogether, this data indicates high internalization of DNCs maintaining

270   intracellular stability of their functional anti-miR fragment over 48 h in HEK293 cells.

271   Next, we sought to investigate the internalization capacity of DNCs in the target cell type of

272   interest for the application of the therapy. In contrast to HEK293, but as expected for primary-like

273   hard-to-transfect cells, human iCMs presented significantly lower (around 10-fold less)

274   internalization capacity of the structures (Figure 5a). Confocal microscopy confirmed the

275   intracellular location of Cy3-labelled M, N$_A$ and N$_B$ in both HEK293 and iCMs (Figure 5b and

276   Figure S10). HEK293 presented a more diffuse intracellular pattern of internalized DNCs than

277   iCMs, supporting the observed differences in uptake capacity between cell types.
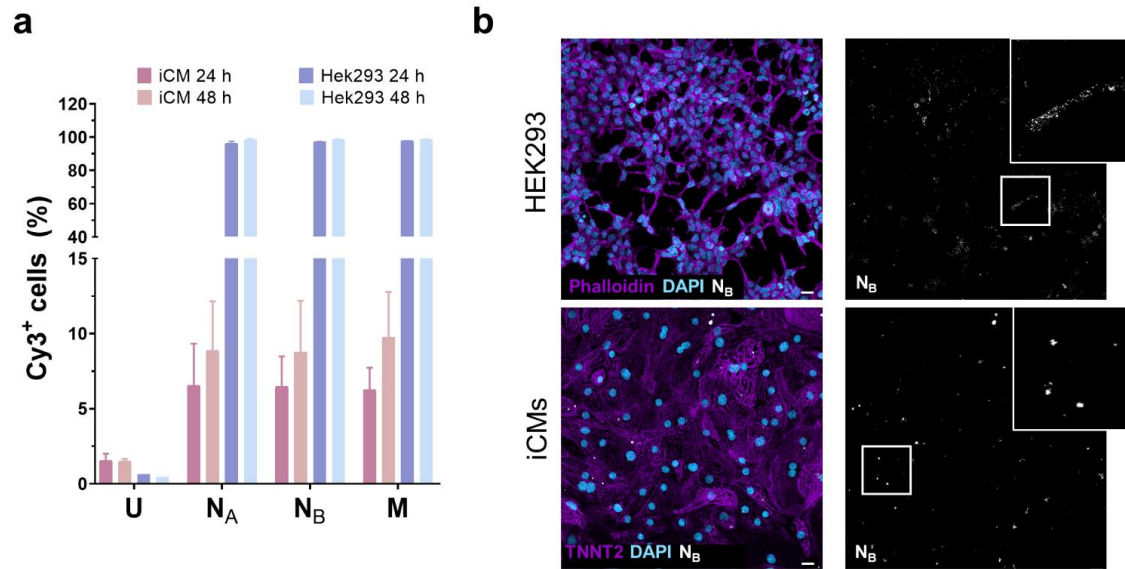
Figure 5. Uptake capacity and subcellular location of DNCs in HEK293 and human iCMs. a) Percentage of $Cy3^+$ cells in both cell types at 24 and 48 h (mean±SD, n=2-3 with 1-2 technical replicates each) treated with DNCs or untreated (U). b) Immunostaining with nuclear counterstain (DAPI), Phalloidin (HEK293, top) and TNNT2 (iCMs, bottom) of cells treated with Cy3-labelled N_B. An orthogonal projection is shown. Scale bar corresponds to 20 µm.

In summary, the assembled DNCs do not alter cell viability in cultured cells and, upon internalization, they maintain their anti-miR bait sequence stable in the intracellular milieu. However, they show remarkably different internalization capabilities depending on the cell type studied. This highlights the opportunity to implement strategies that enhance the cardiac cell-specific uptake of DNCs to achieve on-target efficacy *in vivo*.

DNC functional assessment in a model cell system

Given the reduced internalization of DNCs in human iCMs, we evaluated the functionality of the developed DNCs in model cell systems via luciferase reporter assay (Figure S11). Briefly,

15

294   HEK293 were co-transfected with a luciferase reporter vector containing the *SERCA2* gene

295   sequence (Figure S11a) and either miR-24-2-5p (Figure S11b) or a commercial miR mock

296   (miR$_{mock}$). The miR$_{mock}$ is a miR that does not interact with human mRNAs, so the luciferase

297   activity in this case represents the basal activity of the model. On the other hand, co-transfection

298   of HEK293 with the reporter vector and miR-24-2-5p indicates the degree of inhibition exerted by

299   the miR on SERCA2 expression (relative to the basal activity of miR$_{mock}$), as previously reported[6].

300   These cellular models were treated with N$_A$, N$_B$, M or scramble DNCs (N$_{sc}$) (Figure 6). N$_{sc}$ shares

301   the configuration of N$_A$ and the sequences of M, but with the exception that M$_{sc}$ harbours a random

302   anti-miR sequence that is not complementary to miR-24-2-5p or miR$_{mock}$ (Table S1). Therefore,

303   N$_{sc}$ is a negative control for the specificity of miR-24-2-5p capture. The combination of the

304   miR$_{mock}$ cells with the N$_{sc}$ treatment gives the basal luciferase activity of the model treated with

305   DNCs. With this set up, miR-24-2-5p transfected cells treated with N$_{sc}$ maintained the described

306   level of miR-24-2-5p-mediated SERCA2 inhibition [6] by 0.76 ± 0.03 fold. When assessing the

307   anti-miR-24-5p treatments, N$_B$ and M specifically and significantly restored the luciferase activity

308   to levels not statistically different to the basal condition, with fold changes of 0.93 ± 0.06 and 0.94

309   ± 0.06, respectively. Therefore, N$_B$ and M were able to rescue the miR-24-2-5p-mediated

310   inhibition. Instead, N$_A$ did not have an effect, in agreement with the lower capturing capacity of

311   N$_{A\text{-}LU}$ as compared to N$_{B\text{-}LU}$ by fluorometric analysis (Figure 3 c,d).

312   Overall, this result shows higher functional performance of N$_B$ over the N$_A$ in capturing the target

313   miR intracellularly and validates the ability of N$_B$ to regulate the levels of a potentially pathological

314   cardiac miR *in vitro* using biocompatible DNA nanocarriers.
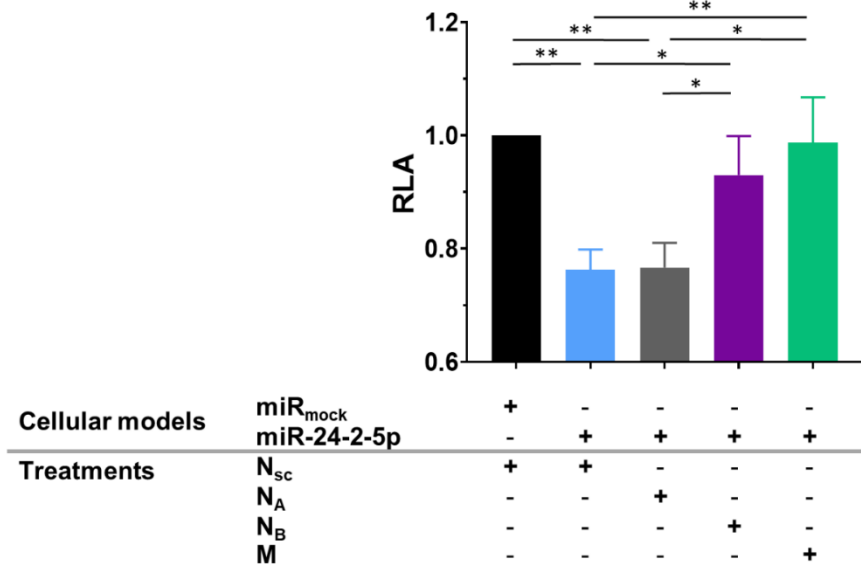
Figure 6. Functional assessment of DNCs in cellular model systems. Relative luciferase activity (RLA) of the *pmiRGLO-SERCA2 vector* reporter vector co-transfected with miR mimics (miR-24-2-5p or miR_{mock}) was determined after 24 h treatment with the different DNCs (mean±SD, n = 3 with 4 technical replicates in each experiment). Significance thresholds were established at: $p \leq 0.05$ (*), $p \leq 0.01$ (**), $p \leq 0.001$ (***) and $p \leq 0.0001$ (****).

CONCLUSION

We have successfully developed and characterized biocompatible anti-miR-loaded DNCs that effectively and specifically capture the target miR-24-2-5p *in vitro*. Our DNCs show stability against nuclease degradation in cell culture media up to 24 h and exhibit the capacity to be internalized by HEK293 cells in a biocompatible manner. While DNCs were also internalized in iCMs, the efficiency was significantly lower than in HEK293 cells. Nonetheless, DNCs, particularly N_B and M, exhibit the ability to restore SERCA2 levels in a cellular model system providing proof of concept of efficacy of a new system with therapeutic potential in HF or age-

330 related cardiac dysfunction. Interestingly, the hybridization strategy employed to form DNCs has

331 a discernible impact on their ability to modulate the miR-24-2-5p effect. Namely, the internal miR

332 bait structure N_B functionally outperforms the 3'-end bait N_A structure, highlighting the

333 significance of DNC design in enhancing its performance capabilities. In addition to providing

334 nuclease protection, the larger size exhibited by N_B compared to M, should benefit retarding renal

335 clearance in systemic delivery[43], making N_B interesting for future *in vivo* studies.

336 Our results suggest that DNCs hold promise as carriers for miR therapies targeting human cardiac

337 cells. As a matter of fact, the observed cell-type specific differences emphasize the prospect

338 towards DNCs functionalization to promote efficient and specific carrier uptake by primary

339 cardiac cells *in vivo*. Strategies to achieve targeted delivery of DNCs to cardiac tissue could exploit

340 the use of heart-specific ligands, such as aptamers[44] or peptides[45,46]. These type of ligands have

341 already demonstrated success in tissue-specific nanoparticle delivery, [47,48] including cardiac

342 targeting.[48] Additionally, the light up system integrated in our DNCs, makes them potentially

343 suitable, upon adequate cardiac-targeting engineering, for *in vivo* preclinical imaging of miR-24-

344 2-5p present in cardiac tissue, and hence interesting for theranostic purposes.

345

346 **MATERIALS AND METHODS**

347 **DNCs design and assembly**

348 The design of DNCs was conducted based on an adaptation from previous reports.[33] Prior to

349 assembly, all DNA sequences underwent analysis using Nupack[49] and BLAST[50] software. The

350 sequences of all used oligonucleotides can be found in Table S1. Unmodified oligos were

351 purchased from IDT (Integrated DNA Technologies, Inc.) and Macrogen, Inc, while labelled

352 oligos were obtained from Biomers.

353   DNCs are composed by three building units: monomer (M), linker (L) and stopper (S). N_A and N_B

354   share the same M unit, but they differ in L and S. In the case of N_A, the 12-nts long extensions of

355   L_A attach via complementary hybridization with the initial 12 nts of the 22-nts long overhangs

356   present in each of the three arms of M. S_A contains only one 12-nts long overhang complementary

357   to the 12-nts long extension of L_A. Regarding N_B, L_B attaches to the final 12-nts overhang present

358   in each of the three arms of M and to the single 12-nts long overhang in S_B.

359   In Cy3-labelled DNCs, 40% of Cy3 labelled M was added to samples for DNCs assembly.

360   Specifically, 40% of M is labelled with one strand fluorescently functionalised with the Cy3

361   fluorophore (Table S1) and 60% of M is added unlabelled. $DNCs_{LU}$ were developed to track

362   ssDNA/ssRNA-mediated disassembly process. To this end, 20% of M_{LU} was Cy3 labelled (present

363   in one of the 3 strands) (table S1) and 100% of L_{LU} are labelled with BMNQ535 quenchers (present

364   in the two strands composing L_{LU}). Note that M_{LU} contains a single Cy3 label, whereas L_{LU} is

365   labelled with two BMN-Q535 quenchers, one per overhang, to ensure complete fluorescence

366   quenching upon assembly.

367   M, S and L were assembled at equimolar oligonucleotide concentration in PBS solution. DNCs

368   were assembled by mixing M, S and L following the ratio 64:1 (M:S), 1:1.5 (M:L) and 2:1 (S:L).

369   These ratios correspond to molar concentrations of 4 μM of M, 62.5 nM of S and 6.031 μM of L.

370   The assembly of DNA nanostructures (M, S, L and the DNCs) was carried out in a thermocycler

371   with a thermal-annealing protocol from 95 to 25 °C in 140 steps (0.5 °C per step, 30 s each step).

372   Samples were stored at 4 ºC.

373

374

375

DNCs structural characterization

Electrophoretic mobility shift assay (EMSA)

EMSA was performed using either PAGE or AGE. For PAGE, 20 ng of each DNA sample were loaded. Samples were run for 1 h at 100 V in an 8% polyacrylamide gel immersed in a solution containing 11 mM $MgCl_2$ buffered with 1x Tris-Acetate-EDTA (TAE) (pH=8.3) (Thermo Fisher, 10628403). As a reference, a 100 bp DNA ladder or 1 Kb DNA ladder (New England Biolabs, N3231 and N3232) were run along with the samples. As for AGE, 50 ng of each DNA sample were loaded. Samples were run for 1 h at 100 V in a 3% agarose gel immersed in an 11 mM $MgCl_2$ 1x TAE running buffer. For subsequent visualization, the gels were stained with GelRed (Biotium, 41003) and imaged under ultraviolet light transillumination.

Dynamic light Scattering (DLS)

The hydrodynamic sizes of M, N_A and N_B were measured by DLS. N_A and N_B were folded in PBS at a concentration of 200 ng/µL and M was folded at a higher concentration of 800 ng/µL (20 µM) due to its smaller size. Samples were analysed at 25 ºC using the Malvern analytical Zetasizer Nano ZS instrument. The reported values represent the average of 5 independent studies of 10 measurement each, consisting of 5 reads per run. Values in intensity are provided.

Atomic Force Microscopy (AFM)

For AFM studies, 4 µL of either M, N_A or N_B at a concentration of 50 ng/µL were spotted onto freshly exfoliated mica and left to adsorb to the surface for 5 minutes. Then, sample was washed thrice with filtered Milli-Q water followed by soaking up of excess water using a tissue and slow drying under a soft air nitrogen steam for 3 minutes. Samples were analysed using a Veeco-Bruker Multimode 8 instrument with NGS30 tips (golden silicon probes, force constant 1.2-6.4 N/m, NT-NMD Spectrum Instruments) in tapping mode in air. Images were analysed using Gwyddion 2.60

399   Software. The diameters of DNA nanostructures were estimated extracting profiles of individual

400   motifs in the two different axes. The value per particle is the averaged of the profiles of the two

401   different axes. 50 motifs were analysed to provide the averaged value.

402   miR capturing study

403   DNCs with the same M concentration (1 µM) were incubated with the ssRNA, ssDNA or

404   ssDNA$_{mock}$ during 1h at 37 ºC at various molar ratios (bait fragment: anti-miR target sequence).

405   Samples were then analysed by PAGE and fluorescence spectrophotometry. PAGE was performed

406   as described above. DNCs$_{LU}$ samples were assembled as described for DNCs. Samples were

407   diluted 1:5 in PBS (final M concentration of 800 nM) and sequences (ssDNA, ssRNA, ssDNA$_{mock}$)

408   were added to a final concentration of 2.4 µM to match the concentration of bait overhangs.

409   Fluorescence was recorded in a ClarioStar plate reader setting the excitation at 540 nm and the

410   emission window from 556 to 696 nm. Fluorescent measurements were recorded at 37 ºC.

411   Fluorescence curves data were processed with Origin software. Fluorescence maxima was fixed

412   at 565 nm.

413   DNAse I and cell culture media mediated DNCs degradation

414   Nuclease degradation of M, N$_A$ and N$_B$ was studied through incubation with either DNase I or

415   DMEM supplemented with 10% FBS (DMEMc). Regarding DNase I degradation study, samples

416   were incubated at a DNA concentration of 50 ng/µL with 4.0 U/mL, 2.0 U/mL, 1.0 U/mL, 0.5

417   U/mL, 0.25 U/mL, 0.125 U/mL and 0 U/mL of DNase I (New England Biolabs, M0303) along

418   with 1x DNase I buffer at 37 ºC for 1h. For the DMEMc degradation study, 50 ng/µL of M, NA

419   and NB were incubated with DMEM (Thermo Fisher, 13476146) supplemented with 10% FBS

420   (Sigma Aldrich, F7524) at 37 ºC during different times: 0h, 1h, 3h, 6h and 24h. All samples were

421   analysed using PAGE. The degree of stability was quantified by measuring the decrease in the

422   intensity of the main band corresponding to the non-degraded DNC and the emergence of a smear

423   resulting from degradation compared to time 0h, using image J. Specifically, the percentage of

424   non-degraded structure was calculated using the following two equations:

425   Eq1. $F = \frac{I}{I+S}$

426   Eq2. % NDS $= \frac{Fi}{F0} \times 100$

427   Where F is the fraction of the main band; I, is the intensity of the main band; S, is the intensity of

428   the slurry; % NDS, is the percentage of non-degraded structure; F_i, is the fraction of the main band

429   at every time point I and F_0, is the fraction of the main band at the initial time point.

430   **Cell culture of HEK293, human induced pluripotent stem cells (iPSC) and differentiation**

431   **towards cardiomyocytes (iCM)**

432   HEK293 cells were maintained in Minimum Essential Media (MEM) (Biowest, BWSTL0415)

433   supplemented with 10% Fetal Bovine Serum (FBS) (Thermo Fisher, 10270106) and 1%

434   Penicillin/Streptomycin   (Thermo   Fisher,   15140122),   according   to   manufacturer's

435   recommendations and passaged regularly when reaching confluence using EDTA 0.5 mM.

436   The human iPSC line Bj1[51], kindly provided by Dr Prof. Verfaillie (Katholieke Universiteit

437   Leuven, Belgium), was cultured on vitronectin- (Thermo Fisher, A14700) coated dishes with

438   Essential 8 medium (Stem Cell Techonologies, 05990) and routinely passaged with EDTA 0.5

439   mM. iPSC seeded at a density of 100000 cells/cm^2 on matrigel (Falcon, 354277) coated-dishes

440   underwent directed differentiation to cardiomyocytes after 48 h following the Giwi protocol

441   established by Lian and colleagues.[52] On day 10, iCMs were enriched and then purified during

442   three days with Cardiomyocyte Purification Medium (CPM), containing RPMI 1640 no glucose

443   (Thermo   Fisher,   11879020),   2%   B27   supplement   (Gibco,   17504001)   and   1%

444   Penicilin/Streptomycin. Finally, iCMs were expanded in cardiomyocyte expansion media (CEM)

445　(RPMI1640 (Biowest, BWSTL0500), 2% B27 Supplement (Thermo Fisher, 17504001)

446　supplemented and with 2 µM CHIR99021 (MERCK, SML1046-5MG) according to Buikema and

447　colleagues.[53,54] Before the addition of DNCs, iCMs were incubated with Cardiomyocyte

448　Maintenance Medium (CMM) based on RPMI1640 (Biowest, BWSTL0500) and 2% B27

449　Supplement (Thermo, 17504044).

450　**Cell viability assays**

451　HEK293 were seeded in a 96-well plate at a density of 60,000 cells/cm^2 and, after 24 h, M, N_A and

452　N_B were added at final concentration of 100 ng/µL of DNA.

453　Immediately, three phase contrast images per well were acquired every 2 h during 48 h at 10x

454　magnification in the Incucyte® SX5 platform (Sartorius). Image analysis was done in the

455　Incucyte® 2021C software by determining the percentage of confluence per well normalized to

456　untreated cells (without DNCs) and normalized to 0 h.

457　**Uptake and intracellular stability by flow cytometry (FC)**

458　The internalization and intracellular stability of DNCs (N_A and N_B) were evaluated in HEK293

459　cells with 50 ng/µL of Cy3-labelled DNCs or 50 ng/µL DNCs$_{LU}$, respectively. HEK293, were

460　seeded in a 96-well plate at a density of 60,000 cells/cm^2. The day after, DNCs were added and

461　incubated for 0.5, 7, 24 and 48 h before analysis in a Gallios Flow Cytometer (Beckman Counter).

462　Uptake capacity was evaluated in HEK293 and iCMs with 100 ng/µL of Cy3-labelled DNCs after

463　24 and 48 h of treatment. HEK293 were prepared as for internalization/intracellular stability

464　analysis. iCMs were plated in 48-well plates coated with Geltrex™ LDEV-Free Reduced Growth

465　Factor Basement Membrane Matrix (Gibco, A1413202), at 60,000 cells/cm^2 and maintained in

466　CEM till nearly confluence. Then, media was replaced by CMM and incubated for another 7 days

467　in CMM to gain maturity before DNCs addition. FC data analysis was performed with FlowJo^{TM}

468   software. Internalization capacity was determined as the percentage of $Cy3^+$ cells while

469   intracellular stability was calculated as the mean fluorescence intensity (MFI) of each DNCs

470   normalized to the MFI of the initial timepoint (0.5 h).

471   **Immunofluorescence and imaging**

472   HEK293 and iCMs were prepared as for FC analysis but plated on 10 mm cover slip and incubated

473   with 100 ng/µL DNCs (M, N_A and N_B) for 24 h before fixation with 4% paraformaldehyde. Then,

474   HEK293 were permeabilized with 0,1% saponin and 1% Bovine Serum Albumin (BSA) (Sigma-

475   Aldrich, A9647) in DPBS, stained with 1:100 dilution of Phalloidin Alexa Fluor® 488 (Thermo

476   Fisher, A12379) in DPBS for 1 hour at room temperature in darkness and finally counterstained

477   with 3µM DAPI for 20 minutes (Abcam, ab228549). iCMs were permeabilized and blocked with

478   0.1%Triton X-100 (CAS 9002-93-1) during 15 minutes and with undiluted protein block (Agilent,

479   X090930-2) during 25 minutes, respectively. After DPBS washing, cells were incubated with a

480   1:100 dilution of primary antibody rabbit anti-Cardiac Troponin I (Abcam, ab91605) overnight at

481   4 ºC. The secondary antibody, Alexa Fluor 488 goat anti-rabbit IgG (Invitrogen, A11034) diluted

482   1:1000, was incubated during 30 minutes in darkness followed by 3µM DAPI counterstaining as

483   indicated previously.

484   Images were acquired with a Carl Zeiss LSM 880 Confocal Microscope (Carl Zeiss, Germany) at

485   40x magnification. Image processing and analysis was performed with ZEN software.

486   **Luciferase reporter assays**

487   HEK293 cells were plated in 384-well plates at a density of 100,000 cells/cm^2 and co-transfected

488   with a SERCA2 luciferase vector[6] (Figure S11) and miR mimics using Lipofectamine 2000

489   Transfection Reagent (Invitrogen, 11668027) according to manufacturer's instructions.

490   Specifically, 45 ng of *pmiRGLO-SERCA2* reporter vector (Figure S11a) and 0.6 pmoles of miR

491   mimic sequences, including hsa-miR-24-2-5p miR Mimic (Cohesion Bioscience, CMH0480) and

492   miR Mimic Negative Control (miR$_{mock}$) (Cohesion Bioscience, CMH0000) were used. The media

493   was changed after 24h post-transfection, and, after another 24 h, cells were incubated with 100

494   ng/µl of N$_A$, N$_B$ or M for 24 h. Also, 100 ng/µl of a DNC with a random bait sequence (N$_{sc}$) was

495   used as negative control (Table S1). Luciferase reporter assays were conducted using the Dual-

496   Glo® Luciferase Assay System (Promega, E2920) following manufacturer's instructions.

497   Luminescence signal produced by the reporter and normalizer proteins, namely Firefly (*Fluc*) and

498   Renilla luciferases, respectively, were measured on the Biotek Synergy HT.

499   Relative luciferase activity (RLA) was calculated as the ratio of each experimental condition to

500   the basal luciferase activity of the model treated with DNCs, namely the miR$_{mock}$ cellular model

501   treated with N$_{sc}$. Luminescence values were determined by normalizing the Fluc relative light units

502   (RLUs) to Renilla RLUs in each well.

503   **Statistical analysis**

504   GraphPad was used for statistical analyses. Data is reported as mean ± standard deviation (SD).

505   One-way ANOVA test was used to compare independent groups. The significance threshold was

506   established at $p \leq 0.05$ (*) and following significance levels were $p \leq 0.01$ (**), $p \leq 0.001$ (***),

507    $p \leq 0.0001$ (****).

508

REFERENCES

[1]   World Health Organization (WHO), "Cardiovascular diseases," **2021**.

[2]   J. L. Rodgers, J. Jones, S. I. Bolleddu, S. Vanthenapalli, L. E. Rodgers, K. Shah, K. Karia, S. K. Panguluri, *J. Cardiovasc. Dev. Dis.* **2019**, *6*, DOI 10.3390/jcdd6020019.

[3]   M. Zhou, G. Zhao, Y. Zeng, J. Zhu, F. Cheng, W. Liang, *Rev. Cardiovasc. Med.* **2022**, *23*, 135.

[4]   R. M. W. Colpaert, M. Calore, *Cells 2019, Vol. 8, Page 737* **2019**, *8*, 737.

[5]   R. A. Boon, K. Iekushi, S. Lechner, T. Seeger, A. Fischer, S. Heydt, D. Kaluza, K. Tréguer, G. Carmona, A. Bonauer, et al., *Nature* **2013**, *495*, 107.

[6]   E. Ramos-Marquès, L. García-Mendívil, M. Pérez-Zabalza, H. Santander-Badules, S. Srinivasan, J. C. Oliveros, R. Torres-Pérez, A. Cebollada, J. M. Vallejo-Gil, P. C. Fresneda-Roldán, et al., *Aging Cell* **2021**, *20*, e13383.

[7]   K. Gabisonia, G. Prosdocimo, G. D. Aquaro, L. Carlucci, L. Zentilin, I. Secco, H. Ali, L. Braga, N. Gorgodze, F. Bernini, et al., *Nature* **2019**, *569*, 418.

[8]   R. Hinkel, D. Ramanujam, V. Kaczmarek, A. Howe, K. Klett, C. Beck, A. Dueck, T. Thum, K. L. Laugwitz, L. Maegdefessel, et al., *J. Am. Coll. Cardiol.* **2020**, *75*, 1788.

[9]   J. Täubel, W. Hauke, S. Rump, J. Viereck, S. Batkai, J. Poetzsch, L. Rode, H. Weigt, C. Genschel, U. Lorch, et al., *Eur. Heart J.* **2021**, *42*, 178.

[10]   E. Van Rooij, L. B. Sutherland, N. Liu, A. H. Williams, J. McAnally, R. D. Gerard, J. A. Richardson, E. N. Olson, *Proc. Natl. Acad. Sci. U. S. A.* **2006**, *103*, 18255.

[11]   J. Wang, W. Huang, R. Xu, Y. Nie, X. Cao, J. Meng, X. Xu, S. Hu, Z. Zheng, *J. Cell. Mol. Med.* **2012**, *16*, 2150.

[12]   T. Ma, F. Qiu, Y. Gong, H. Cao, G. Dai, D. Sun, D. Zhu, H. Lei, Z. Liu, L. Gao, *Theranostics*

2023, *13*, 3826.

[13] L. Zhihao, N. Jingyu, L. Lan, S. Michael, G. Rui, B. Xiyun, L. Xiaozhi, F. Guanwei, *Heart Fail. Rev.* **2020**, *25*, 523.

[14] B. Greenberg, J. Butler, G. M. Felker, P. Ponikowski, A. A. Voors, J. M. Pogoda, R. Provost, J. Guerrero, R. J. Hajjar, K. M. Zsebo, *Gene Ther.* **2016**, *23*, 313.

[15] C. Diener, A. Keller, E. Meese, *Trends Genet.* **2022**, *38*, 613.

[16] M. Cassani, S. Fernandes, J. Vrbsky, E. Ergir, F. Cavalieri, G. Forte, *Front. Bioeng. Biotechnol.* **2020**, *8*, 506432.

[17] C. R. Lucas, P. D. Halley, A. A. Chowdury, B. K. Harrington, L. Beaver, R. Lapalombella, A. J. Johnson, E. K. Hertlein, M. A. Phelps, J. C. Byrd, et al., *Small* **2022**, *18*, 2108063.

[18] B. R. Madhanagopal, S. Zhang, E. Demirel, H. Wady, A. R. Chandrasekaran, *Trends Biochem. Sci.* **2018**, *43*, 997.

[19] L. Zhu, J. Luo, K. Ren, *J. Mater. Chem. B* **2023**, *11*, 261.

[20] J. Huang, W. Ma, H. Sun, H. Wang, X. He, H. Cheng, M. Huang, Y. Lei, K. Wang, *ACS Appl. Bio Mater.* **2020**, *3*, 2779.

[21] Q. Chi, Z. Yang, K. Xu, C. Wang, H. Liang, *Front. Pharmacol.* **2020**, *10*, 1.

[22] S. Raniolo, V. Unida, G. Vindigni, C. Stolfi, F. Iacovelli, A. Desideri, S. Biocca, *Cell Death {\&} Dis. 2021 121* **2021**, *12*, 1.

[23] K. Zhang, J. Liu, Q. Song, X. Yang, D. Wang, W. Liu, J. Shi, Z. Zhang, *ACS Appl. Mater. Interfaces* **2019**, *11*, 46604.

[24] S. Nahar, A. K. Nayak, A. Ghosh, U. Subudhi, S. Maiti, *Nanoscale* **2017**, *10*, 195.

[25] K. Kumari, A. Kar, A. K. Nayak, S. K. Mishra, U. Subudhi, *RSC Adv.* **2021**, *11*, 10670.

[26] A. Kar, K. Kumari, S. K. Mishra, U. Subudhi, *BMC Cancer* **2022**, *22*, 1.

[27] L. Yu, S. Yang, Z. Liu, X. Qiu, X. Tang, S. Zhao, H. Xu, M. Gao, J. Bao, L. Zhang, et al., *Mater. Today Bio* **2022**, *15*, 100276.

[28] D. Shu, H. Li, Y. Shu, G. Xiong, W. E. Carson, F. Haque, R. Xu, P. Guo, *ACS Nano* **2015**, *9*, 9731.

[29] D. W. Binzel, Y. Shu, H. Li, M. Sun, Q. Zhang, D. Shu, B. Guo, P. Guo, *Mol. Ther.* **2016**, *24*, 1267.

[30] S. Li, Y. Liu, T. Zhang, S. Lin, S. Shi, J. He, Y. Xie, X. Cai, T. Tian, Y. Lin, *Adv. Mater.* **2022**, *34*, 2204287.

[31] Y. Luo, X. Yang, Y. Du, Y. Dou, W. Cui, J. Li, J. Wei, X. Ma, Y. Lin, *ACS Appl. Mater. Interfaces* **2023**, *15*, 29813.

[32] S. Osteonecrosis, D. Li, Z. Yang, Y. Luo, X. Zhao, M. Tian, P. Kang, **2022**, *2101412*, 1.

[33] J. Li, C. Zheng, S. Cansiz, C. Wu, J. Xu, C. Cui, Y. Liu, W. Hou, Y. Wang, L. Zhang, et al., *J. Am. Chem. Soc.* **2015**, *137*, 1412.

[34] P. J. Kolbeck, M. Dass, I. V Martynenko, R. J. A. van Dijk-Moes, K. J. H. Brouwer, A. van Blaaderen, W. Vanderlinden, T. Liedl, J. Lipfert, *Nano Lett.* **2023**, *23*, 1236.

[35] W. Song, P. Song, Y. Sun, Z. Zhang, H. Zhou, X. Zhang, P. He, *ACS Biomater. Sci. Eng.* **2021**, *7*, 5165.

[36] L. Eswaran, G. Kazimirsky, G. Byk, *Pharm. 2023, Vol. 15, Page 332* **2023**, *15*, 332.

[37] H. Zhu, J. Wu, J. Zhao, L. Yu, B. R. Liyarita, X. Xu, Y. Xiao, X. Hu, S. Shao, J. Liu, et al., *Acta Biomater.* **2024**, *175*, 240.

[38] Y. Hu, S. Gao, H. Lu, S. Tan, F. Chen, Y. Ke, J. Y. Ying, *Nano Lett.* **2023**, *23*, 9778.

[39] C. Xu, Q. Liu, J. Shi, Z. Liu, Z. Lei, C. Dai, W. Shi, X. Xu, Y. Guo, *ACS Appl. Nano Mater.* **2024**, *7*, 19143.

[40] L. Lauková, B. Konečná, Ľ. Janovičová, B. Vlková, P. Celec, *Biomolecules* **2020**, *10*, 1036.

[41] H. Auvinen, H. Zhang, Nonappa, A. Kopilow, E. H. Niemelä, S. Nummelin, A. Correia, H. A. Santos, V. Linko, M. A. Kostiainen, *Adv. Healthc. Mater.* **2017**, *6*, 1700692.

[42] D. Lysne, T. Hachigian, C. Thachuk, J. Lee, E. Graugnard, *J. Am. Chem. Soc.* **2023**, *145*, 16691.

[43] J. Di, X. Gao, Y. Du, H. Zhang, J. Gao, A. Zheng, *Asian J. Pharm. Sci.* **2021**, *16*, 444.

[44] S. Philippou, N. P. Mastroyiannopoulos, M. Tomazou, A. Oulas, M. Ackers-Johnson, R. S. Foo, G. M. Spyrou, L. A. Phylactou, *Pharmaceuticals (Basel).* **2023**, *16*, 1264.

[45] M. J. McGuire, K. N. Samli, S. A. Johnston, K. C. Brown, *J. Mol. Biol.* **2004**, *342*, 171.

[46] S. Rana, K. Datta, T. L. Reddy, E. Chatterjee, P. Sen, M. Pal-Bhadra, U. Bhadra, A. Pramanik, P. Pramanik, M. Chawla-Sarkar, et al., *J. Control. Release* **2015**, *200*, 167.

[47] C. Liang, B. Guo, H. Wu, N. Shao, D. Li, J. Liu, L. Dang, C. Wang, H. Li, S. Li, et al., *Nat. Med.* **2015**, *21*, 288.

[48] X. Zhao, W. Luo, J. Hu, L. Zuo, J. Wang, R. Hu, B. Wang, L. Xu, J. Li, M. Wu, et al., *J. Nanobiotechnology* **2018**, *16*, 36.

[49] J. N. Zadeh, C. D. Steenberg, J. S. Bois, B. R. Wolfe, M. B. Pierce, A. R. Khan, R. M. Dirks, N. A. Pierce, *J. Comput. Chem.* **2011**, *32*, 170.

[50] S. F. Altschul, W. Gish, W. Miller, E. W. Myers, D. J. Lipman, *J. Mol. Biol.* **1990**, *215*, 403.

[51] L. Ordovás, R. Boon, M. Pistoni, Y. Chen, E. Wolfs, W. Guo, R. Sambathkumar, S. Bobis-Wozowicz, N. Helsen, J. Vanhove, et al., *Stem Cell Reports* **2015**, *5*, 918.

[52] X. Lian, C. Hsiao, G. Wilson, K. Zhu, L. B. Hazeltine, S. M. Azarin, K. K. Raval, J. Zhang, T. J. Kamp, S. P. Palecek, *Proc. Natl. Acad. Sci. U. S. A.* **2012**, *109*, E1848.

[53] J. W. Buikema, S. Lee, W. R. Goodyer, R. G. Maas, O. Chirikian, G. Li, Y. Miao, S. L. Paige, D. Lee, H. Wu, et al., *Cell Stem Cell* **2020**, *27*, 50.

[54] R. G. C. Maas, S. Lee, M. Harakalova, C. J. B. Snijders Blok, W. R. Goodyer, J. Hjortnaes, P. A. F. M. Doevendans, L. W. Van Laake, J. van der Velden, F. W. Asselbergs, et al., *STAR Protoc.* **2021**, *2*, 100334.

ASSOCIATED CONTENT

Supporting Information.

The following files are available free of charge.Brief description; Figures S1-S11 and Table S1. Sequences, complementary data on characterization data of DNCs assembly by GE, DLS and AFM, stability in biological media by GE, miR capturing capacity by GE, schematic representation of light up designs, Tm calculation of DNCs components, FC data, single plane confocal images and further information of the luciferase assay.

AUTHOR INFORMATION

Corresponding Author

Laura Ordovás: lordovas@unizar.es; Silvia Hernández-Ainsa: silviamh83@unizar.es

Author Contributions

The manuscript was written through contributions of all authors. All authors have given approval to the final version of the manuscript. ‡These authors contributed equally.

ACKNOWLEDGMENTS